Inorganic Chemistry
Article

Inorg. Chem. **2011**, *50*, 969–977 **969**
DOI: 10.1021/ic1015934

Investigation of the Electronic, Photosubstitution, Redox, and Surface Properties of New Ruthenium(II)-Containing Amphiphiles

Frank D. Lesh, Marco M. Allard, Rama Shanmugam, Lew M. Hryhorczuk, John F. Endicott, H. Bernhard Schlegel, and Cláudio N. Verani*

Department of Chemistry, Wayne State University, 5101 Cass Avenue, Detroit, Michigan 48202, United States

Received August 6, 2010

A series of pyridine- and phenol-based ruthenium(II)-containing amphiphiles with bidentate ligands of the following types are reported: $[(L^{PyI})Ru^{II}(bpy)_2](PF_6)_2$ (**1**), $[(L^{PyA})Ru^{II}(bpy)_2](PF_6)_2$ (**2**), $[(L^{PhBuI})Ru^{II}(bpy)_2](PF_6)$ (**3**), and $[(L^{PhClI})Ru^{II}(bpy)_2](PF_6)$ (**4**). Species **1** and **2** are obtained by treatment of $[Ru(bpy)_2Cl_2]$ with the ligands L^{PyI} (*N*-(pyridine-2-ylmethylene)octadecan-1-amine) and L^{PyA} (*N*-(pyridine-2-ylmethyl)octadecan-1-amine). The imine species **3** and **4** are synthesized by reaction of $[Ru(bpy)_2(CF_3SO_3)_2]$ with the amine ligands HL^{PhBuA} (2,4-di-*tert*-butyl-6-((octadecylamino)methyl)phenol), and HL^{PhClA} (2,4-dichloro-6-((octadecylamino)methyl)phenol). Compounds **1**−**4** are characterized by means of electrospray ionization (ESI^+) mass spectrometry, elemental analyses, as well as electrochemical methods, infrared and UV−visible absorption and emission spectroscopies. The cyclic voltammograms (CVs) of **1**−**2** are marked by two successive processes around −1.78 and −2.27 V versus Fc^+/Fc attributed to bipyridine reduction. A further ligand-centered reductive process is seen for **1**. The Ru^{II}/Ru^{III} couple appears at 0.93 V versus Fc^+/Fc. The phenolato-containing **3** and **4** species present relatively lower reduction potentials and more reversible redox behavior, along with $Ru^{II/III}$ and phenolate/phenoxyl oxidations. The interpretation of observed redox behavior is supported by density functional theory (DFT) calculations. Complexes **1**−**4** are surface-active as characterized by compression isotherms and Brewster angle microscopy. Species **1** and **2** show collapse pressures of about 29−32 $mN \cdot m^{-1}$, and are strong candidates for the formation of redox-responsive monolayer films.

Introduction

Metallosurfactants comprise a new class of coordination compounds that combine metal properties such as geometric control, redox, optical, and magnetic behavior[1,2] with amphiphilicity.[3] These materials are increasingly relevant for high-end applications involving optoelectronics,[4] logic and memory operations,[5,6] and micellar luminescence and electron transfer.[7,8] Therefore, the integration of amphiphilic properties to antennae constituents is a relevant step toward the development of metallosurfactant precursors for photoresponsive modular films for artificial photosynthesis. In this regard, ruthenium bipyridyl complexes such as the $[Ru^{II}(bpy)_2]^{2+}$ have received considerable attention because of their superior photosensitizing properties and consequent relevance toward water oxidation.

In recent years, our group has spearheaded a comprehensive effort toward redox active precursors for Langmuir−Blodgett films. We have established a wide range of differentiated scaffold designs,[9,10] studied redox and collapse mechanisms,[11] and demonstrated how coordination and protonation preferences dictate amphiphilic behavior.[12]

We have envisioned the integration of the photoresponsive $[Ru^{II}(bpy)_2]^{2+}$ to bidentate amphiphilic ligands containing aminomethyl-pyridine and -phenol headgroups, and in this article, we evaluate a new family of asymmetric $[LRu(bpy)_2]^{+/2+}$ metalloamphiphiles, namely, $[(L^{PyI})Ru^{II}(bpy)_2](PF_6)_2$ (**1**), $[(L^{PyA})Ru^{II}(bpy)_2](PF_6)_2$ (**2**), $[(L^{PhBuI})Ru^{II}(bpy)_2](PF_6)$ (**3**), and $[(L^{PhClI})Ru^{II}(bpy)_2](PF_6)$ (**4**) (Scheme 1), where *Py* = pyridine and

*To whom correspondence should be addressed. Phone: 313 577 1076. Fax: 313 577 8022. E-mail: cnverani@chem.wayne.edu.

(1) Bodenthin, Y.; Pietsch, U.; Mohwald, H.; Kurth, D. G. *J. Am. Chem. Soc*. **2005**, *127*, 3110–3114.
(2) Talham, D. R. *Chem. Rev*. **2004**, *104*, 5479–5502.
(3) Hoogenboom, R.; Fournier, D.; Schubert, U. S. *Chem. Commun*. **2008**, 155–162.
(4) Zhang, J.; Chu, B. W. K.; Zhu, N.; Yam, V. W. W. *Organometallics* **2007**, *26*, 5423–5429.
(5) Low, P. J. *Dalton Trans*. **2005**, 2821–2824.
(6) Wassel, R. A.; Gorman, C. B. *Angew. Chem*. **2004**, *43*, 5120–5123.
(7) Guerrero-Martinez, A.; Vida, Y.; Dominguez-Gutierrez, D.; Albuquerque, R. Q.; De Cola, L. *Inorg. Chem*. **2008**, *47*, 9131–9133.
(8) Wang, K.; Haga, M.; Monjushiro, H.; Akiba, M.; Sasaki, Y. *Inorg. Chem*. **2000**, *39*, 4022–4028.
(9) Shakya, R.; Hindo, S. S.; Wu, L.; Ni, S.; Allard, M.; Heeg, M. J.; da Rocha, S. R.; Yee, G. T.; Hratchian, H. P.; Verani, C. N. *Chem.—Eur. J*. **2007**, *13*, 9948–9956.
(10) Shakya, R.; Keyes, P. H.; Heeg, M. J.; Moussawel, A.; Heiney, P. A.; Verani, C. N. *Inorg. Chem*. **2006**, *45*, 7587–7589.
(11) Shakya, R.; Hindo, S. S.; Wu, L.; Allard, M. M.; Heeg, M. J.; Hratchian, H. P.; McGarvey, B. R.; da Rocha, S. R.; Verani, C. N. *Inorg. Chem*. **2007**, *46*, 9808–9818.
(12) Lesh, F. D.; Hindo, S. S.; Heeg, M. J.; Allard, M. M.; Jain, P.; Peng, B.; Hryhorczuk, L.; Verani, C. N. *Eur. J. Inorg. Chem*. **2009**, 345–356.

Published on Web 01/07/2011

Scheme 1. Series of Pyridine- and Phenolate-Based Ruthenium(II)-Containing Amphiphiles **1**−**4**

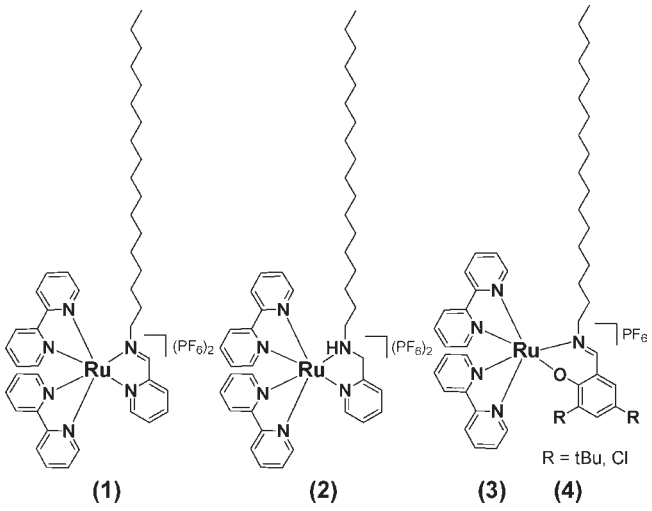

Ph = phenolate, *I* = imine and *A* = amine, and *Bu* or *Cl* indicates the *ortho*- and *para*-substituted *tert*-butyl or chloro groups in the phenolate complexes. We interrogate the electrochemical properties of these systems to evaluate the nature of the redox processes, the optical and electronic properties to evaluate the photostability and excitability (emission) of these species, and the amphiphilic properties to evaluate the potential for formation of ordered LB films. In particular, we evaluate (a) how the presence of C18 alkyl groups allow for formation of high-quality Langmuir films at the air/water interface, (b) the difference in related species (imino versus amino) for L^{Py} and (*tert*-butyl versus chloro) for L^{Ph}, and (c) whether density functional theory (DFT) calculations can model and account for the observed redox responses. These concerns are addressed using a host of synthetic, spectrometric, spectroscopic, and computational- and surface-dedicated methods, and we attempt to correlate these properties to assess the viability of these species as precursors for photoresponsive LB films.

Results and Discussion

Syntheses and Characterizations. Design Rationale. The rationale behind our design strategy involves the combination of distinct donor sets built into photoresponsive $[Ru^{II}(bpy)_2]^{2+}$ moieties by means of bidentate chelating ligands containing hydrophobic alkyl tails. This design is based on our previously described pyridyl-[13−15] and phenol-based[16] ligands coordinated to the Cu(II) dication and bears resemblance to some of the work by Yam et al.[4,17,18] and Keyes et al.[19,20] We aim at extending efforts toward the relatively more inert bivalent Ru^{2+} ion, targeting the electrochemical redox behavior of species **1**−**4**, while preserving their amphiphilic and photoresponsive character. Along with the ligands L^{PyI} and L^{PyA} present in **1** and **2**, we recognized phenolato-based complexes as less prevalent. This prompted us to merge well-established amphiphilic ligands such as HL^{PhBuA} and HL^{PhClA} with $[Ru(bpy)_2]^{2+}$ to yield the imines **3** and **4** with extended spectroscopic and electrochemical features.[19]

Ligands. Condensation of 1-octadecylamine with 2-pyridinecarboxyaldehyde in methanol gave the imine surfactant ligand precursor L^{PyI} which was subsequently reduced in the presence of sodium borohydride to yield the amine ligand precursor L^{PyA}.[15] The phenol-containing surfactant ligands HL^{PhBuA} and HL^{PhClA} were generated from 1-octadecylamine in reaction with 3,5-di-*tert*-butyl-2-hydroxybenzaldehyde or 3,5-dichloro-2-hydroxybenzaldehyde, respectively, followed by reduction to generate the amine precursors.[16] These ligands were characterized by means of ^{1}H NMR and infrared (IR) spectroscopies and electrospray ionization (ESI-MS) mass spectrometry with generally 80−85% overall yields.

Complexes. The Ru(II) pyridine complexes **1**−**2** were obtained by adapting general synthetic approaches for analogous compounds by treatment of equimolar ratios of *cis*-$[Ru(bpy)_2Cl_2]\cdot 2H_2O$ with the ligands L^{PyI} and L^{PyA} in absolute ethanol.[4,17] The Ru(II) phenol-containing metallosurfactantsz **3**−**4** were achieved upon complexation of the ligands HL^{PhBuA} and HL^{PhClA} with $Ru(bpy)_2(CF_3SO_3)_2$ in isopropanol or acetone, respectively, using triethylamine as a base for phenol deprotonation. Because previous attempts using *cis*-$[Ru(bpy)_2Cl_2]\cdot 2H_2O$ led to undesirable side products, $Ru(bpy)_2(CF_3SO_3)_2$ was chosen for complexation with the phenolate-containing ligands. This route took advantage of the excellent leaving group properties of the triflate ion. It should be pointed out that compounds **3** and **4** encompass imine ligands formed from in situ oxidation of the parent amine ligands. Such conversion has been reported in similar systems.[21]

All complexes were precipitated with ammonium hexafluorophosphate and purified by column chromatography to yield microcrystalline powders which were characterized by IR, elemental analyses, ESI^+ mass spectrometry, and electrochemical methods. Elemental analyses for **1**−**4** were in excellent agreement with theoretical percentages. The ESI^+ mass analyses of **1** and **2** in methanol indicate the presence of signature peak clusters with general formulas $[(L^{PyX})Ru^{II}(bpy)_2]^{2+}$ and $[(L^{PyX})Ru^{II}(bpy)_2PF_6]^+$. The phenolate species **3** and **4**, being composed of a charged ligand, showed single mass patterns corresponding to the monovalent $[(L^{PhBuI})Ru^{II}(bpy)_2]^+$ ion species. A differential isotopic distribution was observed for **4** due to the contributing chloride isotopes. The pertinent *m*/*z* peak clusters are shown in

(13) Driscoll, J. A.; Allard, M. M.; Wu, L. B.; Heeg, M. J.; da Rocha, S. R. P.; Verani, C. N. *Chem.—Eur. J.* **2008**, *14*, 9665–9674.
(14) Driscoll, J. A.; Keyes, P. H.; Heeg, M. J.; Heiney, P. A.; Verani, C. N. *Inorg. Chem.* **2008**, *47*, 7225–7232.
(15) Jayathilake, H. D.; Driscoll, J. A.; Bordenyuk, A. N.; Wu, L. B.; da Rocha, S. R. P.; Verani, C. N.; Benderskii, A. V. *Langmuir* **2009**, *25*, 6880–6886.
(16) Hindo, S. S.; Shakya, R.; Rannulu, N. S.; Allard, M. M.; Heeg, M. J.; Rodgers, M. T.; da Rocha, S. R.; Verani, C. N. *Inorg. Chem.* **2008**, *47*, 3119–3127.
(17) Chu, B. W.; Yam, V. W. W. *Inorg. Chem.* **2001**, *40*, 3324–3329.
(18) Yam, V. W. W.; Lee, V. W. M. *J. Chem. Soc., Dalton Trans.* **1997**, 3005–3010.
(19) Keyes, T. E.; Leane, D.; Forster, R. J.; Coates, C. G.; McGarvey, J. J.; Nieuwenhuyzen, M. N.; Figgemeier, E.; Vos, J. G. *Inorg. Chem.* **2002**, *41*, 5721–5732.
(20) Leane, D.; Keyes, T. E. *Inorg. Chim. Acta* **2006**, *359*, 1627–1636.
(21) Lanznaster, M.; Heeg, M. J.; Yee, G. T.; McGarvey, B. R.; Verani, C. N. *Inorg. Chem.* **2007**, *46*, 72–78.

Table 1. Photophysical Parameters for Complexes **1**−**4**

complex	absorption λ_{abs} (nm)/ε (L mol^{-1} cm^{-1})[a]	emission λ_{em}/nm; cm^{-1} [b,c]	lifetime τ_o (ns)[c]
1	239 (17,330); 243 (17,530); 255 (16,030); 287 (44,120); 345 sh (4,460); 432 sh (8,940); 462 (11,080)	715; 13,986	77
2	245 (18,120); 291 (43,850); 342 (7,450); 424 sh (4,540); 472 (7,070)	641; 15,601	193
3	248 (50,260); 294 (59,200); 377 (13,870); 476 sh (7,950); 521 (8,550)		
4	247 (37,910); 295 (60,860); 363 (10,570); 519 (8,380)		

[a] Spectra measured in 1.0×10^{-5} M acetonitrile solution. [b] Emission maxima are corrected values. [c] Excitation wavelength at 460 nm for **1** and 470 nm for **2**.

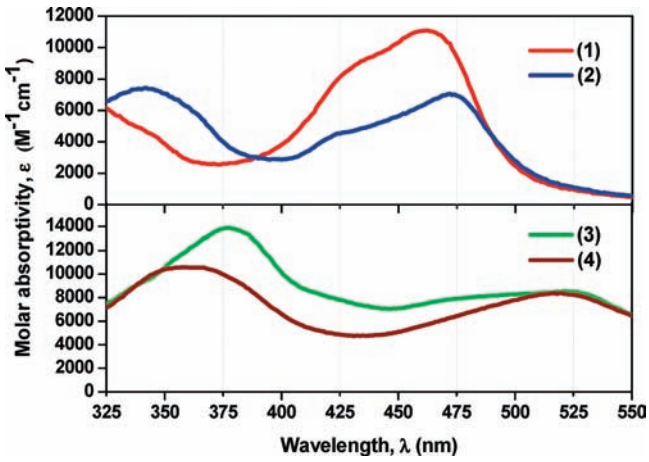

Figure 1. UV−visible spectra of pyridyl complexes **1** and **2** (top) and phenolate complexes **3** and **4** (bottom) in acetonitrile, 1.0×10^{-5} M.

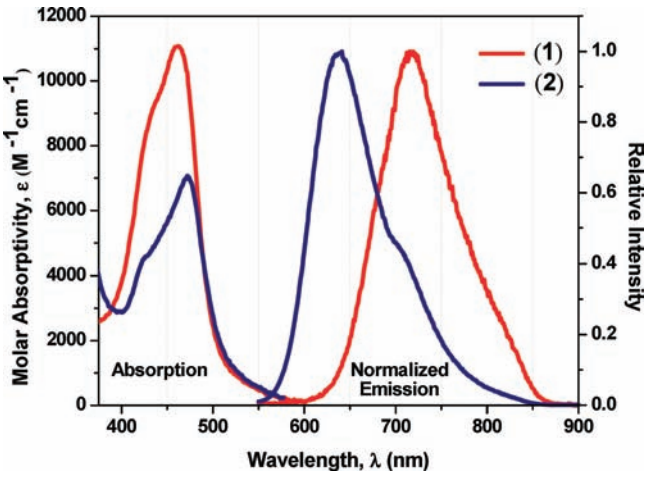

Figure 2. Emission spectra of pyridyl complexes **1** and **2**.

the Supporting Information, Figures S1−S4 and were simulated in good agreement with their patterns, positions, and isotopic distributions.

Complex formation was further observed by the presence of vibrational modes attributed to the ligand, particularly the characteristic strong C−H stretching contribution of the alkyl chain appearing at 2851−2924 cm^{-1}, and the strong stretch at 840−846 cm^{-1} (ν_{P-F}) due to the totally symmetric vibration frequency of hexafluorophosphate counterion.

Electronic Absorption Spectroscopy. Electronic absorption spectral data for complexes **1**−**4** were measured in 10^{-3} to 10^{-5} M acetonitrile solutions. Table 1 lists relevant absorption maxima and molar extinction coefficients, and spectra are displayed in Figure 1. Intense intraligand $\sigma \rightarrow \pi^*$ and $\pi \rightarrow \pi^*$ processes dominate the ultraviolet region of the spectrum for **1**−**4** with two maxima centered about 245 and 290 nm. Appreciably larger absorptivities have been observed for the phenolato-based **3** and **4**. Additionally, a third less intense intraligand absorption band is positioned near 342 nm for the pyridyl-based ligand compounds. A shoulder is seen for **1**; the equivalent band for compounds **3** and **4** is red-shifted to the vicinity of 370 nm. Previously Meyer et al.[22] have isolated and investigated the related $[Ru(bipy)_2(AMPy)](ClO_4)_2$, where (AMPy) is 2-(aminomethyl)-pyridine, analogous to **1**−**2**. A matching absorption profile can be drawn between that species and **2**, allowing to infer that the alkyl chain plays a negligible electronic role to the overall spectroscopic properties of these species. Both the complex $[Ru(bipy)_2(AMPy)](ClO_4)_2$ and **2** exhibit an ill-defined shoulder at 425 nm, absent in the pyridyl-imine **1**, where this corresponding shoulder is slightly shifted to 432 nm. On the basis of other related compounds,[4,17,18,22] we tentatively ascribe this band to a composite of allowed intraligand $\pi \rightarrow \pi^*$ and $d\pi(Ru^{II}) \rightarrow \pi^*$(bpy) metal-to-ligand charge transfer transitions. The second feature of importance in the visible region is a broad band transition at 462 nm for **1**. This transition band is attributed to the $d\pi(Ru^{II}) \rightarrow \pi^*$(iminomethylpyridine) metal-to-ligand charge transfer transition,[4,17,18,22] which in the pyridyl-amine **2** is red-shifted to 472 nm with distinctly lower absorptivity. The overall smaller ligand-field strengths of the σ-donating phenolato ligands present comparatively red-shifted, markedly broad low-energy metal-to-ligand charge-transfer (MLCT) or intraligand CT bands for complexes **3** and **4**, relative to **1** and **2** containing the π-acceptor pyridyl ligands. These charge transfer transitions are observed at 519−521 nm (ε = 8380−8550 L mol^{-1} cm^{-1}) for both **3** and **4**, thus consistent with the behavior observed for other RuN_5O chromophores in similar ligand-donor environments.[23,24]

Emission Spectroscopy. Room temperature (RT) excitation of **1** and **2** in acetonitrile at $\lambda > 460$ nm induces emission at 715 and 641 nm, respectively (Figure 2). The pseudo-Stokes shift for **1** (ca. 7700 cm^{-1}) is about 2100 cm^{-1} larger than that observed for **2** (ca. 5600 cm^{-1}). Species **2** showed a room-temperature lifetime 2.5 times longer than that of **1**. These observations lead to the inference that the lowest energy triplet MLCT states originate from different chromophores, as will be supported by the electrochemical data and

(22) Brown, G. M.; Weaver, T. R.; Keene, F. R.; Meyer, T. J.; Kenan, W. R., Jr. *Inorg. Chem.* **1976**, *15*, 190–196.

(23) Chakraborty, S.; Walawalkar, M. G.; Lahiri, G. K. *J. Chem. Soc., Dalton Trans.* **2000**, 2875–2883.

(24) Holligan, B. M.; Jeffery, J. C.; Norgett, M. K.; Schatz, E.; Ward, M. D. *J. Chem. Soc., Dalton Trans.* **1992**, 3345–3351.

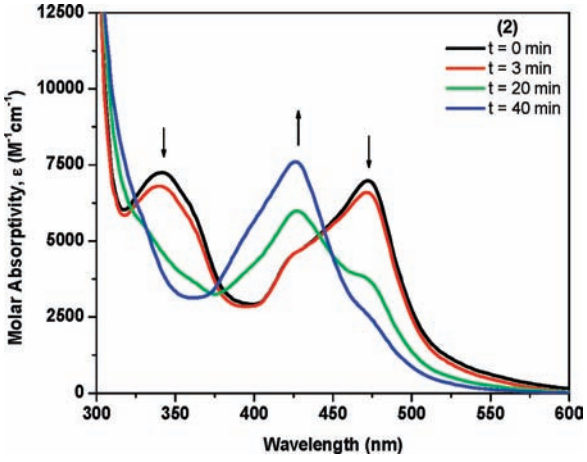

Figure 3. UV−visible spectra recorded for photodissociation of **2** in MeCN.

density functional theory (DFT) calculations. Further studies are necessary for a definitive assignment. The phenolate-based **3** and **4** seem non-emissive in the UV−visible range accessible to the detector at room-temperature in acetonitrile. The $[Ru(bpy)_2(AMPy)](PF_6)_2$ compound was prepared according to the protocol published by Meyer.[22] This species is analogous to the above-mentioned pyridyl-amine complex **2** but lacks the octadecyl chain. The response for both compounds is identical in position and intensity.

Photolability Studies. Owing to the commonly observed photoactive nature of ruthenium-containing complexes, we examined the relative photolability of **1**−**3**. Samples were prepared in dry acetonitrile or dichloromethane to distinguish between the effects of coordinating versus non-coordinating solvents on the apparent photolability of the ruthenium complex. Clear photochemical conversion was observed in complex **2** by the disappearance of peaks at 342 and 472 nm, along with the appearance of a new peak at 427 nm. The observations indicate that **2** was converted into the $[(MeCN)_2Ru^{II}(bpy)_2]^{2+}$ species in acetonitrile (Figure 3).

ESI^+ mass spectrometry supports these results with the appearance of a new peak at $m/z = 248.2$ associated with the dicationic species $[(MeCN)_2Ru^{II}(bpy)_2]^{2+}$. Peaks of interest for **2** and $[(MeCN)_2Ru^{II}(bpy)_2]^{2+}$ were monitored at different cone voltages (5, 20, and 40 V) and times (0, 3, 20, 40 min). At low cone voltages (5 V), the peak at $m/z = 248.2$ increased over time to 100% intensity. Other relevant peaks appeared after 20 min irradiation at $m/z = 641.2$ for $[(MeCN)_2Ru^{II}(bpy)_2 + PF_6]^+$ and $m/z = 361.6$ for $[L^{PyA} + H^+]$, concomitant to a decreased intensity for $m/z = 919.7$ associated with $[\mathbf{2} - PF_6]^+$ and $m/z = 387$ from $[\mathbf{2} - (PF_6)_2]^{2+}$. The $[\mathbf{2} - (PF_6)]^+$ ion disappears after 40 min of photoirradiation. The observed isotopic fingerprint clusters were in good agreement with the nature and charge of the ions present.

The mass spectroscopic results from the photosubstitution experiments for **1**−**2** in acetonitrile were plotted as percentage intensity counts versus time (minutes). For **2**, the decrease in percentage abundance of the $[(L^{PyA})Ru^{II}(bpy)_2 + (PF_6)]^+$ species at a cone voltage of 5 V followed concurrent increase in formation for the $[(MeCN)_2Ru^{II}(bpy)_2]^{2+}$ photoproduct (Supporting Information, Figure S5). A viable photodissociative mechanism has been proposed by Matsuo et al.[25] using online electrospray MS, and seems to involve formation of monodentate intermediates of **2** before the ligand L^{PyA} is fully exchanged by coordinating acetonitrile molecules.

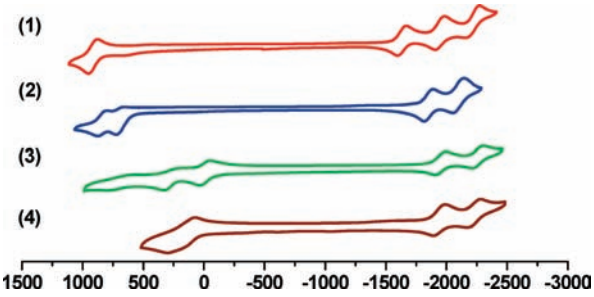

Figure 4. CVs of **1**−**4** in acetonitrile, $TBAPF_6$, versus Fc^+/Fc.

When the non-coordinating dichloromethane was used, no significant changes in the UV−visible and ESI^+ features of **2** were observed (Supporting Information, Figure S6). Furthermore, both **1** and **3** revealed excellent photostability in acetonitrile and dichloromethane. The stability of **3** is tentatively associated to the strong σ-donor nature of the phenolate moiety.[20]

Electrochemistry. The cyclic voltammograms (CVs) of **1**−**4** demonstrate two successive cathodic waves, ranging between $E_{1/2} = -1.78$ and -2.27 V, for the one-electron processes attributed to the classical bipyridine reduction couples (Figure 4). Complex **1** reveals a third ligand-centered reductive process at $E_{1/2} = -2.22$ V versus Fc^+/Fc. The process observed at $E_{1/2} = -1.63$ V versus Fc^+/Fc is tentatively ascribed to the reduction of the L^{PyI} imine-based ligand, which appears at the least negative potential of all complexes. A single quasi-reversible one-electron metal-centered Ru^{II}/Ru^{III} couple appears at $E_{1/2} = 0.93$ V ($\Delta E_p = 0.08$ V; $|I_{pc}/I_{pa}| = 1.31$) versus Fc^+/Fc. The pyridyl-amine based complex **2** displays an irreversible metal-centered oxidative process credited to the Ru^{II}/Ru^{III} couple, as an anodic wave observed at $E_{1/2} = 0.68$ V versus Fc^+/Fc, where $\Delta E_p = 0.12$ V. Additionally, this complex shows a ligand-based process due to the oxidation of the ligand from aminomethylpyridine to its imine counterpart. This oxidative dehydrogenation mechanism was investigated by Keene et al.[22,26,27] The conversion of an amine into an imine is catalyzed by the coordination to the ruthenium ion, and its reversibility seems highly dependent on the scan rate.

Complexes **3** and **4** present more negative potentials for the reductive bipyridine couples, in contrast to the pyridyl-based complexes **1** and **2**. The averaged reduction potentials are $E_{1/2} = -1.94$ and -2.25 V versus Fc^+/Fc, and are comparable in reversibility to those containing aminomethylpyridine ligands. The metal-based $Ru^{II/III}$ oxidation couple and the phenolate/phenoxyl radical ligand oxidative processes are associated with the anodic waves observed for complexes **3** and **4**. These waves have not been assigned conclusively and heavy orbital-interaction between redox centers is most likely a major complicating

(25) Arakawa, R.; Tachiyashiki, S.; Matsuo, T. *Anal. Chem.* **1995**, *67*, 4133–4138.
(26) Keene, F. R.; Ridd, M. J.; Snow, M. R. *J. Am. Chem. Soc.* **1983**, *105*, 7075–7081.
(27) Ridd, M. J.; Keene, F. R. *J. Am. Chem. Soc.* **1981**, *103*, 5733–5740.

Table 2. Cyclic Voltammetry Data for **1**−**4**[a]

	$E_{1/2}$ (ΔE_p) [V], $\lvert I_{pc}/I_{pa}\rvert$	
complex	reductions[b]	oxidations[c]
1	−1.63 (0.09), |1.57|; −1.94 (0.09), |1.56|; −2.22 (0.1)	0.93 (0.08), |1.31|
2	−1.78 (0.06), |0.66|; −2.03 (0.06), |0.91|	0.68 (0.12); 0.93 (0.08)
3	−1.95 (0.09), |1.34|; −2.27 (0.08), |2.02|	−0.01 (0.08); 0.28 (0.10); 0.71 (0.18), |1.44|
4	−1.93 (0.09), |1.65|; −2.23 (0.09), |1.51|	∼ 0.18 (0.20); 0.25^{ox}

[a] CVs of **1**−**4** at 1.0×10^{-3} mol L^{-1} in MeCN with 0.1 M $TBAPF_6$ supporting electrolyte using 150 mV s^{-1} scan rate at RT in an inert atmosphere. [b] Potentials listed as the cathodic peak potential E_{pc} versus Fc^+/Fc. [c] Potentials listed as the anodic peak potential E_{pa} versus Fc^+/Fc. ox = oxidation only

factor for these oxidative type processes. The chloro-substituted complex **4** displays narrowly overlapping oxidative processes. This indicates some destabilization effects on the phenolate-to-phenoxyl oxidation when compared to the *tert*-butyl-substituted complex **3**. Table 2 summarizes the results with potentials reported versus the Fc^+/Fc couple. The correlation of the observed spectroscopic and electrochemical data to the frontier orbitals was explored by means of DFT calculations to understand the origin of these processes.

Electronic Structure Calculations. Representative models **1′**, **2′**, **3′**, and **4′** composed of shortened propyl chains were designed to offer insight into the electronic and structural properties of **1**−**4** (Supporting Information, Figure S7). The models are in good agreement with corresponding structural data of pyridyl- and phenol-based $[Ru^{II}(bpy)_2]$ complexes previously reported.[24,26,28−30] Similar approaches in our group[9,11,12,14,16,31] have been instructive to provide information of the binding modes of metal-containing amphiphilic compounds.

Nature of the HOMOs and LUMOs. Frontier orbitals for **1′**−**4′** were calculated for correlation to and probing of the origin of the observed electrochemical (redox) and spectroscopic (optical) properties.[28] Relative Molecular Orbital (MO) energies are displayed in Figure 5, Supporting Information, Table S1 and Figure S8.

As ordinarily observed for polypyridyl complexes, the contributions from the first three occupied orbitals for the pyridyl-imine based model **1′** can be assigned to the $Ru_{d\pi}$ orbitals. More specifically, the highest occupied molecular orbital (HOMO), HOMO-1, and HOMO-2 are comparatively similar in energy with 74−83% localization on the metal ion. Although the orientation of HOMO-2 is slightly different, the HOMO, HOMO-1, and HOMO-2 orbitals for **2′** are quite consistent to the arrangement observed for **1′**. Interestingly, the three lowest unoccupied molecular orbitals (LUMOs) for **1′** are distinctly unique among the presented series. These three orbitals display similar energy, rather than the typical set of symmetrical and unsymmetrical combinations for bipyridines. The LUMO is dominated by 70% localized contribution of the pyridine-imine ligand, while the LUMO+1 and LUMO+2 are, respectively, the antisymmetric and symmetric combinations of the bipyridine orbitals. In

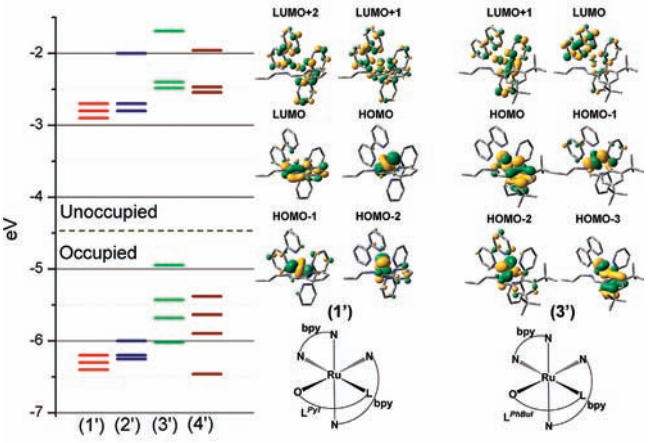

Figure 5. Relative molecular orbital energies.

contrast, the LUMO and LUMO+1 for **2′** are ascribed to the conventional antisymmetric and symmetric combinations of the bipyridine orbitals. The model complexes containing phenolato-based ligands (**3′** and **4′**) behave in a generally comparable manner to one another. However, these complexes consist of different occupied orbital compositions relative to **1′** and **2′**. The HOMO for **3′** is 63% localized on the phenolate-imine based ligand and 31% contribution is coming from a ruthenium-based orbital. The result is a largely mixed metal−ligand orbital. Moreover, the HOMO-1 and HOMO-2 are chiefly $Ru_{d\pi}$-based orbitals with 76% and 69% contributions, respectively, possessing unsuited spatial orientation for overlap with the phenolate pπ-type orbital. Percent compositions of representative MOs are shown in Figure 6 and the Supporting Information, Figure S9.

The HOMO and HOMO-3 appear to be the result of π interactions where the HOMO-3 (45: 46% phenolate-to-metal) is the bonding orbital and the HOMO is described by an antibonding arrangement (Scheme 2).

Correlations to Spectroscopic and Electrochemical Data. Considerable differences in the behavior of **1**−**4** have been observed experimentally. Frontier orbital arguments invoking **1′**−**4′** can be helpful to infer which MOs are related to redox and spectroscopic processes. This approach should be used with caution, considering that orbitals are determined without nuclear relaxation while electrochemistry is an equilibrium measurement. Further complexity is brought to this picture when multiple redox centers are involved. The electrochemical and the DFT-calculated HOMO−LUMO gap are tabulated in Table 3 and plotted in the Supporting Information, Figure S10. The experimental data agrees well with the theoretically calculated trend where **3′** < **4′** < **2′** ≈ **1′**.

(28) Allard, M. M.; Odongo, O. S.; Lee, M. M.; Chen, Y.-J.; Endicott, J. F.; Schlegel, H. B. *Inorg. Chem.* **2010**, *49*, 6840–6852.
(29) Cai, P.; Li, M. X.; Duan, C. Y.; Lu, F.; Guo, D.; Meng, Q. J. *New J. Chem.* **2005**, *29*, 1011–1016.
(30) Chakraborty, S.; Walawalkar, M. G.; Lahiri, G. K. *Polyhedron* **2001**, *20*, 1851–1858.
(31) Shakya, R.; Imbert, C.; Hratchian, H. P.; Lanznaster, M.; Heeg, M. J.; McGarvey, B. R.; Allard, M.; Schlegel, H. B.; Verani, C. N. *Dalton Trans.* **2006**, 2517–2525.

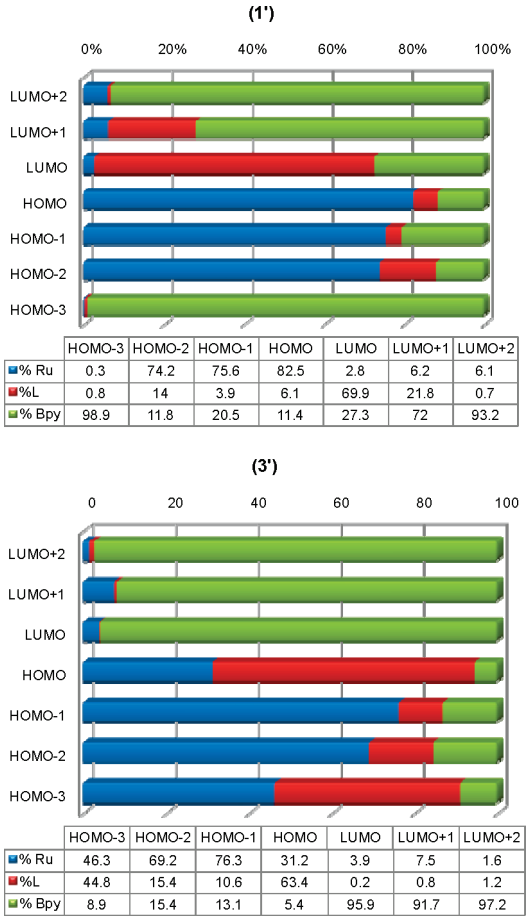

	HOMO-3	HOMO-2	HOMO-1	HOMO	LUMO	LUMO+1	LUMO+2
% Ru	0.3	74.2	75.6	82.5	2.8	6.2	6.1
%L	0.8	14	3.9	6.1	69.9	21.8	0.7
% Bpy	98.9	11.8	20.5	11.4	27.3	72	93.2

	HOMO-3	HOMO-2	HOMO-1	HOMO	LUMO	LUMO+1	LUMO+2
% Ru	46.3	69.2	76.3	31.2	3.9	7.5	1.6
%L	44.8	15.4	10.6	63.4	0.2	0.8	1.2
% Bpy	8.9	15.4	13.1	5.4	95.9	91.7	97.2

Figure 6. Orbital composition for **1′** and **3′**.

Scheme 2. Ru/Phenolate Orbital Interactions for **3′** and **4′**

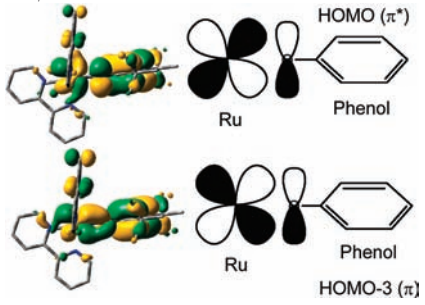

Table 3. Experimental and Calculated HOMO-LUMO Gaps

complex	experimental redox gap (V)[a]	model	calculated HOMO−LUMO gap (eV)[b]
1	2.56	**1′**	3.3
2	2.46	**2′**	3.3
3	1.94	**3′**	2.5
4	2.11	**4′**	2.8

[a] Difference between half-wave potentials for oxidation and reduction. [b] B3LYP/LANL2DZ with IEF-PCM MeCN.

The *tert*-butyl-phenolate species presents the lowest HOMO−LUMO gap (ΔE_{calc} = 2.5 eV, ΔE_{exp} = 1.94 V), and both of the pyridyl-based complexes demonstrate comparable energy values. The differences observed can be directly attributed to the HOMO orbital associated with the anodic oxidation potential. Thus, the oxidative processes must be described as involving heavily mixed Ru-phenolato processes, rather than as formal Ru^{II}/Ru^{III} or phenolate/phenoxyl redox couples. This interpretation is supported by the MLCT bands of **3** and **4** between 500 and 550 nm, where a similar trend is observed as a consequence of a small HOMO−LUMO energy difference.

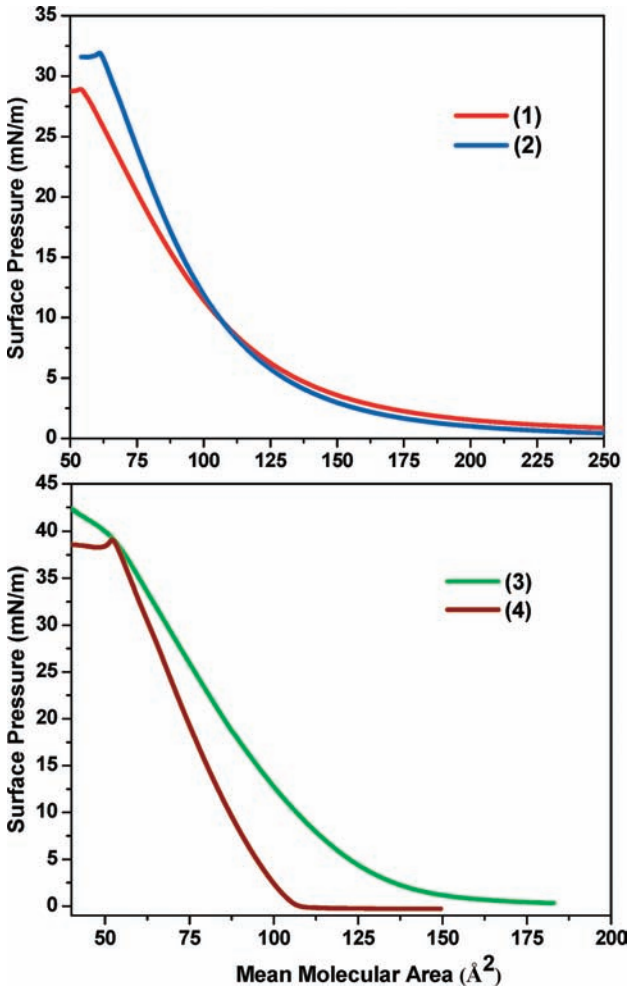

Figure 7. Compression isotherms of the metallosurfactants.

Amphiphilic Properties. The amphiphilic behavior of the metallosurfactants **1**−**4** was analyzed by means of compression isotherms[32] (Figure 7) and Brewster angle microscopy (BAM).[33,34] Langmuir film formation is monitored following the spreading of solutions of the amphiphiles, dissolved in an immiscible organic solvent, onto the aqueous subphase of a minitrough with moveable barriers. As these barriers move closer to each other, compression isotherms plotting surface pressure (Π, mN·m^{-1}) versus average molecular area (A, Å^2) grant fundamental information concerning the two-dimensional molecular organization of the monolayer at the air/water interface, collapse pressures (π_c), limiting areas per molecule (A_{lim}), and monolayer collapse areas (A_c). Simultaneously Brewster angle microscopy evaluates film homogeneity, domain and agglomerate formation upon passing vertically polarized light through media possessing different refractive indexes.

(32) Petty, M. C. *Langmuir-Blodgett Films: An Introduction*; Cambridge University Press: Cambridge, 1996.
(33) Mobius, D. *Curr. Opin. Colloid Interface Sci.* **1998**, *3*, 137–142.
(34) Vollhardt, D. *Adv. Colloid Interface Sci.* **1996**, *64*, 143–171.

Given that the pyridyl-containing ruthenium amphiphiles **1** and **2** showed some solubility in water, complex dissolution was prevented by using a 0.1 M NaCl aqueous subphase with increased ionic strength. The compression isotherms measured for **1** and **2** indicate the formation of well-defined condensed phase regions and distinct collapse pressures; properties characteristic of the formation of stable monolayer films. The individual molecules of both pyridyl-containing amphiphiles start interacting at the air/water interface at an area of about 235 $Å^2 \cdot \text{molecule}^{-1}$ to form an expanded phase. No phase transitions were observed, and **1** presents a collapse pressure of about 29 $mN \cdot m^{-1}$, while **2** shows a collapse pressure of about 32 $mN \cdot m^{-1}$. Amphiphiles **1** and **2** both demonstrate a sudden decrease in surface pressures, which is a trait typical of constant-area collapse mechanisms.[35,36] Collapse areas for these species were obtained by extrapolating the steepest portion of the isotherm to zero pressure, which have been determined to be 125 and 120 $Å^2 \cdot \text{molecule}^{-1}$ for **1** and **2**, respectively. Close structural resemblances can be attributed to the similar interactions observed by the molecules of both complexes at the air/water interface.

Isothermal compressions for the phenolato-containing ruthenium amphiphiles **3** and **4** were recorded in a 0.1 M NaCl aqueous subphase. Although these species are insoluble in water, this subphase was selected to keep consistency. Single molecules of the *tert*-butyl-substituted **3** start interacting at the air/water interface at about 170 $Å^2 \cdot \text{molecule}^{-1}$, whereas the molecules of the chloro-substituted **4** interact at a lower area of about 107 $Å^2 \cdot \text{molecule}^{-1}$. These species do not show distinct phase transitions and display well-defined condensed phase regions until the collapse pressure is reached. Similar surface collapse pressures of about 39 $mN \cdot m^{-1}$were observed for **3** and **4**. However, the *tert*-butyl-substituted **3** shows an isothermal profile akin to a constant-pressure collapse mechanism, and the chloro-substituted counterpart **4** presents a constant-area collapse mechanism. Both mechanisms follow the Ries sequence[37,38] of folding, bending, and breaking into multilayers. Amphiphile **4** confers a moderately sharp area of interaction relative to the other complexes in this series. The limiting areas per molecule for **3** and **4** reach about 120 and 100 $Å^2 \cdot \text{molecule}^{-1}$, respectively. The similar limiting areas per molecule for **1**−**4** are greater than the expected values and can be accounted for by the increased ionic strength of the subphase, suggesting some tilting of the alkyl-chains.[13]

Representative Brewster angle micrographs have been recorded simultaneously along with the isothermal compressions for **1**−**4** (Figures 8 and 9). Complexes **1** and **2** reveal multiple domains before compression and at pressures lower than 4 $mN \cdot m^{-1}$. The pyridyl-imine complex **1** exhibits a smooth and homogeneous film throughout compression. Formation of minor domains at about 29 $mN \cdot m^{-1}$ suggest collapse, directly correlating to the isothermal compression data. Likewise, the pyridyl-amine complex **2** shows a homogeneous monolayer until collapse is reached at about 32 $mN \cdot m^{-1}$. The molecules of the phenolate-containing **3** and **4** form random domains before compression and evolve to smooth, non-corrugated films. At a pressure of about 35 $mN \cdot m^{-1}$ collapse is evident via the formation of several spots interpreted as either Newton rings or vesicles suggestive of thermodynamic film instability.[39]

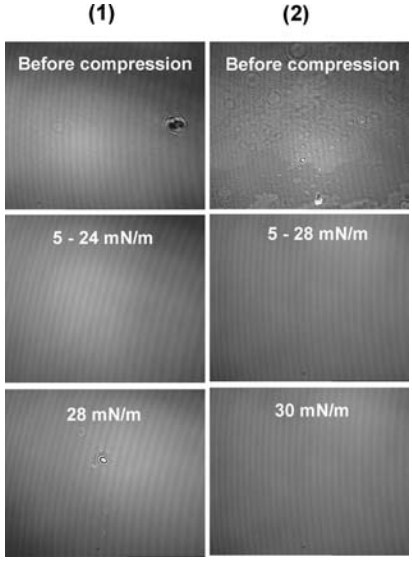

Figure 8. BAM images of complexes **1** and **2**.

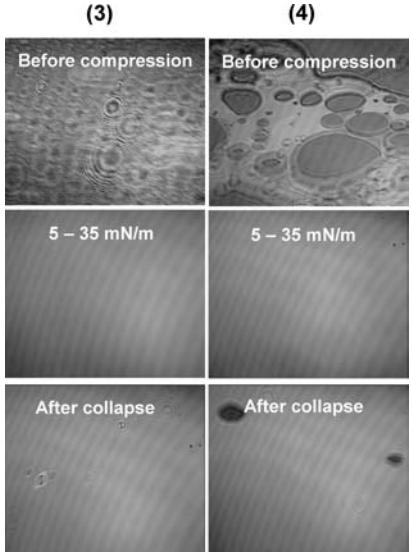

Figure 9. BAM images of complexes **3** and **4**.

Overview and Conclusions

In this article we have described the synthesis and characterization of the new family of pyridyl- and phenolato-containing amphiphiles described as $[(L^{PyI})Ru^{II}(bpy)_2](PF_6)_2$ (**1**), $[(L^{PyA})Ru^{II}(bpy)_2](PF_6)_2$ (**2**), $[(L^{PhBuI})Ru^{II}(bpy)_2](PF_6)$ (**3**), and $[(L^{PhClI})Ru^{II}(bpy)_2](PF_6)$ (**4**). The viability of these species as precursors for photoresponsive Langmuir−Blodgett films was evaluated by addressing (i) the electronic properties to assess the photostability and excitability (emission), (ii) the

(35) Kundu, S.; Datta, A.; Hazra, S. *Phys. Rev. E* **2006**, *73*, 051608/1–051608/7.
(36) Vaknin, D.; Bu, W.; Satija, S. K.; Travesset, A. *Langmuir* **2007**, *23*, 1888–1897.
(37) Ries, H. E., Jr. *Nature* **1979**, *281*, 287–289.
(38) Ybert, C.; Lu, W.; Moller, G.; Knobler, C. M. *J. Phys.: Condens. Matter* **2002**, *14*, 4753–4762.
(39) Galvan-Miyoshi, J.; Ramos, S.; Ruiz-Garcia, J.; Castillo, R. *J. Chem. Phys.* **2001**, *115*, 8178–8184.

electrochemical properties to evaluate the nature of the redox processes, and (iii) the amphiphilic properties to investigate the potential for formation of ordered Langmuir−Blodgett films.

(i). Electronic Properties. Absorption spectral data show the visible region dominated by $d\pi(Ru^{II}) \rightarrow \pi^*$(bpy) MLCT transitions for **1** and **2**, along with $d\pi(Ru^{II}) \rightarrow \pi^*$(iminomethylpyridine) processes for **1**. The pyridylamine **2** shows a red-shifted band at 472 nm. The phenolato complexes **3** and **4** present less intense and red-shifted MLCT observed between 519−521 nm. Emission spectral data show that species **1** and **2** emit at 715 and 641 nm, respectively, with the second species having a lifetime 2.5 times longer than the first. The relative photolability of these species was examined. Clear photochemical conversion was observed for **2** in acetonitrile, but not in dichloromethane. On the basis of ESI^+ mass spectrometric methods, we suggested that **2** was converted into $[(MeCN)_2Ru^{II}(bpy)_2]^{2+}$. The imines **1**, **3**, and **4** do not show evidence of photodissociation.

(ii). Electrochemical Properties. Species **1**−**4** showed rich redox chemistry, where two successive cathodic waves were attributed to bipyridine reduction. More negative potentials for these processes were observed for **3** and **4**, whereas an additional process was observed for **1** and ascribed to the reduction of the imine-based L^{PyI} ligand. Anodic waves were associated to metal oxidation in **1**−**4** and the formation of phenoxyl radicals for **3** and **4**. DFT calculations based on models **1′**−**4′** with shortened propyl chains have helped in the interpretation of the experimental electronic and redox behavior of **1**−**4**. The calculated HOMO−LUMO energy differences correlate well with the observed electrochemical potentials as follows: (a) the energy differences observed for **1** and **2** when compared to **3** and **4**, are directly attributed to the HOMO orbital associated with the oxidation processes, (b) the distinctive three low-lying unoccupied LUMO orbitals for **1′** seem consistent with the electrochemical and emission spectroscopy results, and (c) for **3** and **4**, the oxidative processes are based on heavily mixed Ru-phenolate based MOs that correlate to broad low energy MLCT bands.

(iii). Amphiphilic Properties. Species **1**−**4** are surface-active and are strong candidates for the formation of monolayer films, as characterized by compression isotherms and Brewster angle microscopy. The collapse pressures are fairly high at about 29−32 $mN \cdot m^{-1}$ for **1** and **2** and about 39 $mN \cdot m^{-1}$ for **3** and **4**. Relative solubility in water for **1** and **2** requires the presence of a NaCl aqueous subphase for proper film formation.

Knowledge gained from this effort provides relevant insight toward the integration of amphiphilic properties in the design of photoresponsive precursors for modular films aimed at artificial photosynthetic processes. Our laboratories are currently working on the deposition of Langmuir−Blodgett (LB) films and their photophysical characterization. Integration of [catalytic centers/antennae] into LB films is also under development.

Experimental Section

Materials and Methods. Reagents and solvents were used as received from commercial sources. Methanol was distilled over CaH_2, and dichloromethane was doubly purified on alumina columns using an Innovative Technologies solvent purification system. Infrared spectra were measured from 4000 to 400 cm^{-1} on a Tensor 27 FTIR spectrophotometer in KBr pellets. ^1H NMR spectra were measured with Varian 300 and 400 MHz instruments. ESI(positive) spectra were measured in a triple quadrupole Micromass QuattroLC mass spectrometer with ESCi source. Elemental analyses were performed by Midwest Microlab, Indianapolis, IN. Absorption UV−visible spectroscopy from 1.0×10^{-3} to 1.0×10^{-5} M acetonitrile solutions were performed using a Cary 50 spectrometer within the 250 to 1100 nm range. Fluorescence excitation and emission spectra were measured on a Cary Eclipse fluorescence spectrophotometer. Lifetime measurements were recorded using a Hamamatsu R9220 type photomultiplier tube and decay traces were collected using a National Instruments PCI-5154 digitizer. Samples were excited using a Photochemical Research Associates Inc. nitrogen/dye laser combination LN1000 and LN107, respectively. Lifetimes were determined by single exponential fitting of the luminescence decay traces. Cyclic voltammetry experiments were performed in 1.0×10^{-3} M dry acetonitrile analyte solutions containing 0.1 M $TBAPF_6$ supporting electrolyte using a BAS 50W voltammetric analyzer at a scan rate of 150 $mV\ s^{-1}$. A standard three-electrode cell was employed with a carbon working electrode, a Pt-wire auxiliary electrode, and an Ag/AgCl reference electrode under an inert atmosphere at RT. All potentials are reported versus the Fc^+/Fc internal standard reference couple.[40]

Computational Methods. Electronic structure calculations were carried out with the Gaussian 09 suite of programs[41] using DFT. Calculations with the B3LYP[42−44] functional employed the LANL2DZ[45] basis set and pseudopotential. Since all of the ground states were closed shell singlets, calculations were carried out with spin restricted methods. Tight self-consistent field (SCF) convergence (10−8 rms for the density) was used throughout. Geometries were fully optimized without symmetry constraints, and stationary points were verified via frequency analysis. Solvent effects in acetonitrile were estimated using the IEF-PCM polarizable continuum model.[46−48] Molecular orbitals were plotted with GaussView.[49]

Photolability Studies. Irradiation of dissolved samples **1**−**3** was performed with a highly intense T-type halogen source (500 W) without use of an UV cutoff filter. Photoirradiation of each sample at 1.0×10^{-3} M concentrations occurred in a 25 mL round-bottom flask, fitted with a reflux condenser, under argon

(40) Gagne, R. R.; Koval, C. A.; Lisensky, G. C. *Inorg. Chem.* **1980**, *19*, 2854–2855.
(41) Frisch, M. J.; Trucks, G. W.; Schlegel, H. B.; Scuseria, G. E.; Robb, M. A.; Cheeseman, J. R.; Scalmani, G.; Barone, V.; Mennucci, B.; Petersson, G. A.; Nakatsuji, H.; Caricato, M.; Li, X.; Hratchian, H. P.; Izmaylov, A. F.; Bloino, J.; Zheng, G.; Sonnenberg, J. L.; Hada, M.; Ehara, M.; Toyota, K.; Fukuda, R.; Hasegawa, J.; Ishida, M.; Nakajima, T.; Honda, Y.; Kitao, O.; Nakai, H.; Vreven, T.; Montgomery, J. A.; Peralta, J. E.; Ogliaro, F.; Bearpark, M.; Heyd, J.; Brothers, J. E.; Kudin, K. N.; Staroverov, V. N.; Kobayashi, R.; Normand, J.; Raghavachari, K.; Rendell, A.; Burant, J. C.; Iyengar, S. S.; Tomasi, J.; Cossi, M.; Rega, N.; Millam, J. M.; Klene, M.; Knox, J. E.; Cross, J. B.; Bakken, V.; Adamo, C.; Jaramillo, J.; Gomperts, R.; Stratmann, R. E.; Yazyev, O.; Austin, A. J.; Cammi, R.; Pomelli, C.; Ochterski, J. W.; Martin, R. L.; Morokuma, K.; Zakrzewski, V. G.; Voth, G. A.; Salvador, P.; Dannenberg, J. J.; Dapprich, S.; Parandekar, P. V.; Mayhall, N. J.; Daniels, A. D.; Farkas, O.; Foresman, J. B.; Ortiz, J. V.; Cioslowski, J.; Fox, D. J. *Gaussian G09*; Gaussian,Inc.: Wallingford, CT, 2009.
(42) Becke, A. D. *J. Chem. Phys.* **1993**, *98*, 5648–5652.
(43) Lee, C.; Yang, W.; Parr, R. G. *Phys. Rev. B* **1988**, *37*, 785–789.
(44) Miehlich, B.; Savin, A.; Stoll, H.; Preuss, H. *Chem. Phys. Lett.* **1989**, *157*, 200–206.
(45) Dunning, T. H.; Hay, P. J. In *Modern Theoretical Chemistry*; Plenum: New York, 1976; Vol. *3*, pp 1−28.
(46) Cossi, M.; Rega, N.; Scalmani, G.; Barone, V. *J. Comput. Chem.* **2003**, *24*, 669–681.
(47) Miertus, S.; Scrocco, E.; Tomasi, J. *Chem. Phys.* **1981**, *55*, 117–129.
(48) Miertus, S.; Tomasi, J. *Chem. Phys.* **1982**, *65*, 239–245.
(49) Whangbo, M.-H.; Schlegel, H. B.; Wolfe, S. *J. Am. Chem. Soc.* **1977**, *99*, 1296–1304.

blanketing and stirring for a time period of 40 min while keeping constant the exposure intensity of irradiation. During this time period aliquots were analyzed at times $t = 0, 3, 20$, and 40 min by UV−visible spectroscopy and mass spectrometry.

Isothermal Compression and Brewster Angle Microscopy. Monolayer studies were carried out using an automated KSV 200 mini trough at a temperature of 18 ± 0.5 °C. Since compounds **1** and **2** are found to be partially soluble in the pure water subphase, a 0.1 M NaCl solution (pH ≈ 5.0) was prepared using ultrapure water (Barnstead NANOpure) with a resistivity of about 18.2 MΩ·cm^{-1} and was used as the subphase in each of the experiments. The surface of the subphase was cleaned by vacuum suction after barrier compression. Spreading solutions of a known concentration (1.0 mg·mL^{-1}) and a known quantity (30 μL), prepared in spectra grade chloroform, were then introduced on the clean aqueous subphase. The system was then allowed to equilibrate for 15 min before monolayer compression. The compression isotherms were obtained at a compression rate of 10 mm·min^{-1}. The surface pressure was measured using the Wilhelmy plate (paper plates 20 mm × 10 mm) method. The selected isotherms represent the average of at least three independent measurements with excellent reproducibility. Brewster angle micrographs were taken simultaneously with the compression isotherm using a KSV-Optrel BAM 300 equipped with a HeNe laser (10 mW, 632.8 mm) and a CCD detector. The field of view was 800 × 600 μm and the lateral resolution was about 1 μm.

Syntheses. Preparation of the Ligands L^{PyI}, L^{PyA}, HL^{PhBuA}, and HL^{PhClA}. The ligands were synthesized according to the literature or used as purchased from the commercial source.[15,16] General synthetic approaches for complexes **1**−**4** followed modifications of previously published procedures.[4,14,17] The starting complex $Ru(bpy)_2(CF_3SO_3)_2$ was prepared according to the reported procedure.[50]

Preparation of the Metallosurfactants $[(L^{PyI})Ru^{II}(bpy)_2](PF_6)_2$ (1) and $[(L^{PyA})Ru^{II}(bpy)_2](PF_6)_2$ (2). A 10 mL EtOH solution of *cis*-$[Ru(bpy)_2Cl_2]\cdot 2H_2O$ (0.520 g, 1.0 mmol) was added dropwise to a 30 mL EtOH solution containing either L^{PyI} (0.394 g, 1.1 mmol) or L^{PyA} (0.397 g, 1.1 mmol). In each instance, the resulting mixtures were stirred under mild reflux overnight (24 h) under an argon blanketing atmosphere and protected from light. The solution was filtered while warm to eliminate unreacted solids, and the filtrate was concentrated to half of the original volume by rotary evaporation. Slow solvent evaporation after the addition of a saturated solution of NH_4PF_6 in MeOH precipitated the crude product which was filtered and washed with cold distilled water. The compound was purified by column chromatography using a neutral alumina column with toluene-acetonitrile (2:1) as eluent. The solvent was removed, and the product was dissolved in acetone. Slow solvent evaporation yielded an isolable dark red crystalline powder after drying under vacuum.

1. Yield: 76%. Elemental anal. calcd for $[C_{44}H_{58}F_{12}N_6P_2Ru_1]$: C, 49.76, H, 5.50, N, 7.91%. Found: C, 49.83, H, 5.44, N, 7.89%. IR data (KBr, cm^{-1}): 3084(w) (C−H_{arom}); 2920(s), 2851(s) (alkyl chain C−H stretches); 1606(m) (C=N_{pyr}); 1466(s) (C=C_{arom}); 1162(m) (−C-N-); 846(s) (PF_6^-). UV−visible data (ACN, 1.0×10^{-5} M): 239 (17 330), 243 (17 530), 255 (16 030), 287 (44 120), 345 sh (4460), 432 sh (8940), 462 (11 080). ^{1}H NMR (400 MHz, $CDCl_3$): δ 8.97 (d, 4H), 8.42 (d, 1H), 8.34 (d, 4H), 7.96 (d, 1H), 7.71−7.63 (m, 6H), 7.58 (s, 1H), 7.41 (t, 4H), 1.25 (m, 34H), 0.88 (t, 3H). MS data (ESI$^+$ in MeOH): m/z = 386 (100%) for $([(L^{PyI})Ru^{II}(bpy)_2]^{2+})/+2$, m/z = 917 for $[(L^{PyI})Ru^{II}(bpy)_2 + (PF_6^-)]^+$, and m/z = 771 for $[(L^{PyI})Ru^{II}(bpy)_2]^{2+} - H^+$.

2. Yield: 79%. Elemental anal. calcd for $[C_{44}H_{60}F_{12}N_6P_2Ru_1]$: C, 49.67, H, 5.68, N, 7.90%. Found: C, 49.21, H, 5.68, N, 7.95%. IR data (KBr, cm^{-1}): 3670(w), 3287(w) (N−H); 3086(w) (C−H_{arom}); 2924(s), 2853(s) (alkyl chain C−H stretches); 1604(m) (C=N_{pyr}); 1467(s), 1446(s) (C=C_{arom}); 1162(m) (−C-N-); 840(s) (PF_6^-). UV−visible data (ACN, 1.0×10^{-5} M): 245 (18 120), 291 (43 850), 342 (7450), 424 sh (4540), 472 (7070). ^{1}H NMR (400 MHz, $CDCl_3$): δ 9.06 (d, 4H), 8.50−8.42 (m, 5H), 8.35 (m, 5H), 8.06 (d, 1H), 7.52 (t, 1H), 7.40 (t, 4H), 4.44 (s, 2H), 1.97 (t, 2H), 1.74 (s, 1H), 1.24 (m, 32H), 0.88 (t, 3H). MS data (ESI$^+$ in MeOH): m/z = 387 (100%) for $([(L^{PyA})Ru^{II}(bpy)_2]^{2+})/+2$, m/z = 919 for $[(L^{PyA})Ru^{II}(bpy)_2 + (PF_6^-)]^+$, and m/z = 773 for $[(L^{PyA})Ru^{II}(bpy)_2]^{2+} - H^+$.

Preparation of the Metallosurfactants $[(L^{PhBuI})Ru^{II}(bpy)_2](PF_6)$ (3) and $[(L^{PhClI})Ru^{II}(bpy)_2](PF_6)$ (4). A 10 mL isopropanol or acetone solution of $Ru(bpy)_2(CF_3SO_3)_2$ (0.356 g, 0.5 mmol) was added dropwise to a 30 mL isopropanol or acetone solution containing either HL^{PhBuA} (0.244 g, 0.5 mmol) or HL^{PhClA} (0.222 g, 0.5 mmol), respectively, and Et_3N as base (0.076 g, 0.75 mmol) for deprotonation. Isolation and purification procedures were similar to those of **1** and **2**.

3. Yield: 72%. Elemental anal. calcd for $[C_{53}H_{74}F_6N_5O_1P_1Ru_1]$: C, 61.02, H, 7.15, N, 6.71%. Found: C, 61.25, H, 7.35, N, 6.69%. IR data (KBr, cm^{-1}): 3120(w), 3078(w) (C−H_{arom}); 2922(s), 2857(s) (alkyl chain and *tert*-butyl C−H stretches); 1602(m) (C=N_{pyr}); 1465(s), 1442(s), 1423(s) (C=C_{arom}); 1260(m), 1234(m) (C−O); 1161(m) (−C-N-); 841(s) (PF_6^-). UV−visible data (ACN, 1.0×10^{-5} M): 248 (50 260), 294 (59 200), 377 (13 870), 476 sh (7950), 521 (8550). ^{1}H NMR (400 MHz, $CDCl_3$): δ 8.71 (d, 4H), 8.22 (d, 4H), 8.05 (s, 1H), 7.83 (t, 4H), 7.75−7.73 (s, 2H), 7.41 (t, 4H), 3.15 (t, 2H), 1.24 (m, 50H), 0.88 (t, 3H). MS data (ESI$^+$ in MeOH): m/z = 898 (100%) for $[(L^{PhBuI})Ru^{II}(bpy)_2]^+$.

4. Yield: 70%. Elemental anal. calcd for $[C_{48}H_{64}Cl_2F_6N_5O_2P_1Ru_1]$: C, 54.39, H, 6.09, N, 6.61%. Found: C, 54.60, H, 6.05, N, 6.25%. IR data (KBr, cm^{-1}): 3121(w), 3077(w) (C−H_{arom}); 2923(s), 2852(s) (alkyl chain C−H stretches); 1602(w) (C=N_{pyr}); 1459(s), 1442(s), 1418(s) (C=C_{arom}); 1262(m) (C−O); 1172(m) (−C-N-); 842(s) (PF_6^-). UV−visible data (ACN, 1.0×10^{-5} M): 247 (37 910), 295 (60 860), 363 (10 570), 519 (8380). ^{1}H NMR (400 MHz, $CDCl_3$): δ 8.62 (d, 4H), 8.36 (d, 4H), 8.19 (s, 1H), 8.11 (t, 4H), 7.92−7.84 (s, 2H), 7.45 (t, 4H), 3.67 (t, 2H), 1.25 (m, 32H), 0.88 (t, 3H). MS data (ESI$^+$ in MeOH): m/z = 856 (100%) for $[(L^{PhClI})Ru^{II}(bpy)_2]^+$.

Acknowledgment. This research was made possible by the Division of Chemical Sciences, Geosciences, and Biosciences, Office of Basic Energy Sciences of the U.S. Department of Energy (DOE-BES) through the SISGR-Solar Energy Program Grant DE-FG02-09ER16120 to C.N.V., J.F.E., and H.B.S. Support to F.D.L., M.M.A., and R.S. is acknowledged. Computer time allocated at the WSU-Grid System for the DFT calculations is also acknowledged.

Supporting Information Available: Experimental and simulated ESI$^+$ peak cluster profiles for **1**−**4**, and for the photosubstitution products in acetonitrile, UV−visible spectra for the recorded photostability of **2** in DCM, schematics for representative DFT models, calculated orbital compositions and energies, the correlation between experimental and calculated half-wave potentials, and the Cartesian coordinates for the optimized structures. This material is available free of charge via the Internet at http://pubs.acs.org.

(50) Greaney, M. A.; Coyle, C. L.; Harmer, M. A.; Jordan, A.; Stiefel, E. I. *Inorg. Chem.* **1989**, *28*, 912–920.